doi: 10.82124/CEAS-GNC-2026-078

EuroGNC
Madrid, Spain May 5th-7th 2026

Contact Force Simulation and Reduction during Robot Assisted Landings of Unmanned Aerial Vehicles

Jannes Terlau Research Assistant, FH Aachen, Faculty of Aerospace and Automotive Engineering, 52064 Aachen, Germany. terlau@fh-aachen.de

Philipp Kremer Research Assistant, FH Aachen, Faculty of Aerospace and Automotive Engineering, 52064 Aachen, Germany. philipp.kremer@fh-aachen.de

Tobias Ostermann Professor, FH Aachen, Faculty of Aerospace and Automotive Engineering, 52064 Aachen, Germany. tobias.ostermann@fh-aachen.de

Philipp Hartmann Professor, FH Aachen, Faculty of Aerospace and Automotive Engineering, 52064 Aachen, Germany. p.hartmann@fh-aachen.de

ABSTRACT

This paper presents an approach on contact force simulation and subsequent reduction during robot-assisted landings of unmanned aerial vehicles. The considered landings are performed using a serial kinematic industrial robot with a custom gripper. The goal is to investigate robot-assisted landings for heavier and larger combinations of unmanned aerial vehicles and industrial robots. For that, a multi-body simulation including all involved subsystems is developed, enabling the analysis of the physical interaction between robot and aircraft during the robot-assisted landing. The simulation features contact force calculation capabilities, applying the linear Kelvin-Voigt contact model. The results show an initial rise in contact forces that might pose a structural problem for robot or aircraft. Therefore, the paper proposes an approach on contact force reduction by reducing the relative speed between UAV and gripper at impact. The multi-body simulation is verified based on exemplarily contact situations. By reducing the impact speed, the contact forces are reduced considerably.

Keywords: Contact Force Simulation, Robot Assisted Landing, Unmanned Aerial Vehicle, Multi-Body Simulation

Nomenclature

F_c = Contact force
k = Spring stiffness
d = Damping
ζ = Damping ratio
q = Joint angle
v_{rel} = Impact speed
v_z = UAV's descent speed
w = Transition length
x = Penetration depth

Except where otherwise noted, content of this paper is licensed under a Creative Commons Attribution 4.0 International License.

The reproduction and distribution with attribution of the entire paper or of individual pages, in electronic or printed form, including any material under non-CC-BY 4.0 licenses is hereby granted by the authors and respective copyright owners.

1 Introduction

The research project CatchUp aims to develop infrastructure that enables safe and efficient landing processes for vertical take-off and landing (VTOL) aircraft. Generally, landing and take-off are considered the most critical phases in aviation. The landing processes of VTOLs require only a small deviation of the desired state of motion and are therefore highly susceptible to disturbances such as gusts. Due to possible delays in conventional ground or flight processes, such landings make it difficult to integrate VTOLs into commercial airports. To speed up landing processes for seamless integration of Advanced Air Mobility (AAM) vehicles into existing airport infrastructure and processes, CatchUp investigates an active ground system that catches the aircraft in flight, utilizing an unmanned aerial vehicle (UAV) as a demonstrator. The ground system serves as a starting point for subsequent ground handling processes. As a result, the landing process becomes more predictable, requires less space and turnaround processes may be automated. Within the project, a 6-axis industrial robot is used for catching a UAV. A custom gripper is attached to the robot's end effector for catching and handling the UAV. The process of catching the UAV has already been demonstrated in a previous project [1], utilizing a model predictive controller to synchronize the robot's movements with the UAV. CatchUp aims to evaluate the approach of robot-assisted landings for heavier and larger combinations of UAV and robot, which may possess different mechanical properties such as inertia or structural stiffness as well as a robot system with less degrees of freedom. To achieve that, the utilized UAV and robot will mimic the behavior of heavier and larger systems. Using heavier and larger combinations of UAV and robot, elastic behavior and structural problems may become non-negligible, disturbing the commanded system behavior, especially during contact situations involving non-static loads. To analyze contact situations, this paper presents the design, creation and exemplary application of a multi-body simulation for robot-assisted landings. The simulation can be used to investigate magnitudes of contact forces between UAV and robot, while respecting both elastic behavior of the involved subsystems as well as sudden changes in the system's inertia after a successful catch. Furthermore, the simulation allows for the design and analysis of control methods to perform robot assisted landings for different combinations of UAV and robot.

2 Related work

Previous work in the field of robot assisted landing of UAVs has already investigated different approaches. In 2016, a landing platform as a part of a DHL parcel station was developed [2]. A tilt-wing UAV with a wingspan of 2 m could be moved on the parcel station's landing platform with a sliding mechanism to replace the battery and payloads. The necessary landing area of such an UAV with no active catching mechanism was identified in [2] as $3\,\text{m} \times 3\,\text{m}$. Another area of research concerning robot assisted landing processes are landings on ships, with a particular focus on landings with rough sea conditions. In [3], a review of different approaches for autonomous landings on ships was presented. For example in [4–7], Maier et al. investigated the capture of a hovering UAV using a robotic arm. In contrast to a free capture process, the UAV was attached to a ball bearing. Therefore, only the last phase of the robot assisted landing process was examined, in which a coordinated deceleration of the UAV and the robotic arm took place. Based on this, an approach was proposed to distribute the workload, enabling landing processes of heavy rotorcraft, whose weight would otherwise exceed the nominal payload of the robot. During this research activity the approach and the actual capture process of the UAV were not considered. In [8], Wu et al. presented an unmanned surface vehicle (USV) equipped with a robotic manipulator built for handling UAVs in maritime domains. Although it employs a similar sensing and control strategy as presented here, the work lacks research results from physically catching the aircraft. In 2022, the company Quantum-Systems GmbH started developing a ground platform as part of the FreeRail research project [9] which is conceptually similar to the approach we employ by using an unmanned tilt-rotor UAV and a robotic arm. However, publicly available videos do not discuss contact force simulation or reduction.

Except where otherwise noted, content of this paper is licensed under a Creative Commons Attribution 4.0 International License.

The reproduction and distribution with attribution of the entire paper or of individual pages, in electronic or printed form, including any material under non-CC-BY 4.0 licenses is hereby granted by the authors and respective copyright owners.

Modeling and analyzing contact forces during landing is a non-trivial task, since the UAV dynamics and the contact force onset occur on widely separated time scales. The resulting equations are referred to as stiff ordinary differential equations (ODEs). Standard numerical techniques may exhibit instability, when solving stiff ODEs. Thus, appropriate numerical methods need to be employed when solving for contact forces during landing. A common application of contact force analysis is the design and layout of aircraft landing gear to ensure compliance with regulations. For this purpose, specialized multi-body simulation tools such as *MSC Adams* or *Simscape* are utilized [10, 11]. Simulation of contact forces for robot assisted landings of UAVs is less common. Ni et al. investigated the landing stability of an adaptive landing gear for UAVs [12]. In their study, a Kelvin-Voigt contact model [13, p. 27] was used to analyze the impact forces during a drop test. In contrast to pure elastic contact force models, the Kelvin-Voigt contact model comprises dissipative processes, considering the energy loss during contact. In comparison to other dissipative models (e.g. Hunt-Crossley, Lankarani-Nikravesh, etc. [13, p. 29-46]), the Kelvin-Voigt model portrays a simple linear approximation of resulting contact forces, satisfactory for analyzing a contact force simulation's plausibility.

3 Fundamentals

The process of a robot assisted landing is based on multiple functionalities, such as estimating the UAV's pose, establishing a communication with the UAV or actuating the robot's and gripper's joints. To design a simulation environment for contact force analysis during the robot assisted landing, key components regarding the catching process need to be identified. Non-key components are part of the system architecture but are not or only loosely connected to the contact force analysis and hence not in the focus of the paper. The following section is divided into an illustration of the overall system architecture followed by a description of the key components for the simulation.

3.1 System architecture

The architecture of the robot system comprises sensor, actuator and processing components. Fig. 1

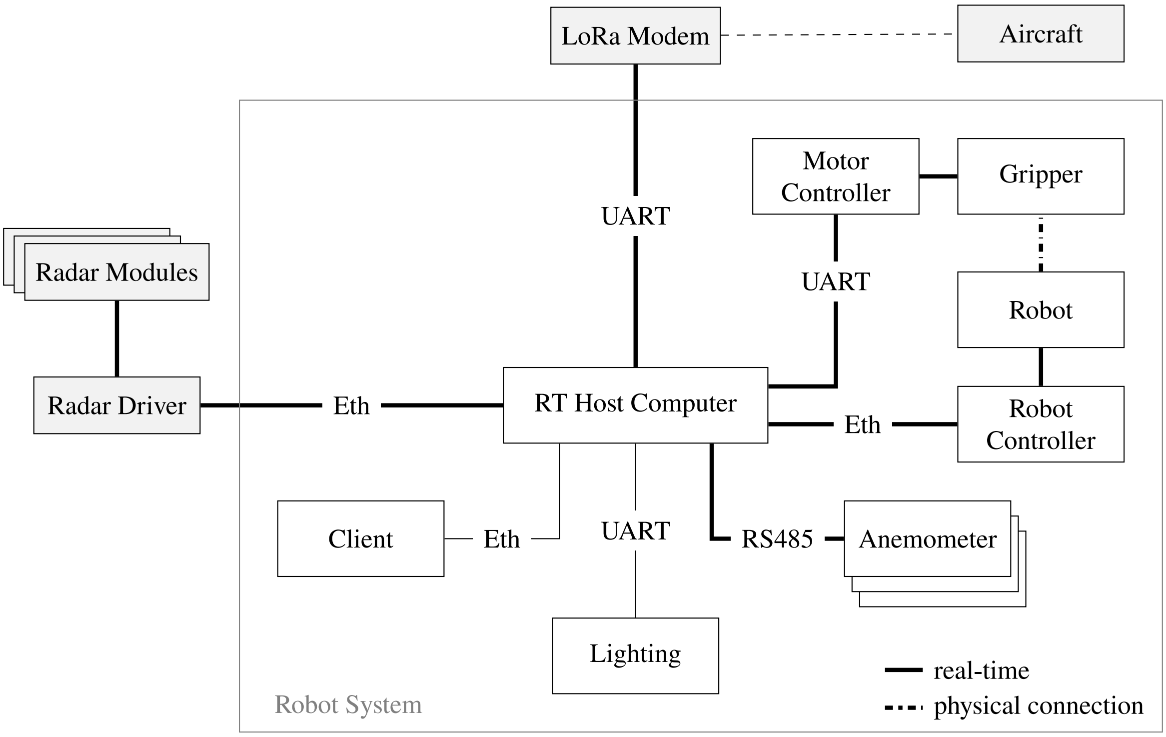

Fig. 1 Architecture of the robot system

Except where otherwise noted, content of this paper is licensed under a Creative Commons Attribution 4.0 International License.

The reproduction and distribution with attribution of the entire paper or of individual pages, in electronic or printed form, including any material under non-CC-BY 4.0 licenses is hereby granted by the authors and respective copyright owners.

visualizes the connections and communication protocols between the corresponding components. Gray shaded parts display external components, provided by project partners. Previous work featured a similar architecture approach [14, p. 6]. However, two changes have been made. First, the optical tracking system for the measurement of the aircraft's pose was exchanged by a radar system. This increases robustness and continuity of the pose estimation, since the influence of environmental factors like the weather condition is reduced. The pose estimation is performed by a Kalman filter aided by the UAV's telemetry, as described in [14, p. 8]. Secondly, the number of employed anemometer was increased. Previously, the robot was able to traverse its task space significantly faster than the expected UAV movements, resulting in robustness against disturbances due to short-term increased wind velocities. When investigating heavier and larger combinations of UAV and robot, where the robot's movement capabilities and the expected UAV movements do not scale linearly, disturbances due to wind may become non-negligible. Thus, increasing the number of locally employed anemometer, the prediction of short-term increased wind velocity can be explored, potentially allowing to compensate for the wind-induced movement of the UAV during the catching process.

3.2 Key components

A first approach on contact force analysis does only consider the physical devices which are in contact with each other. Concurrently, further system components such as the UAV's pose measurement and estimation are simplified and the simulation of other peripherals such as anemometer neglected. Later on, the simulation will enable the stepwise integration of these components, allowing for a representative investigation with the complete system's information flow. A cutout of the system architecture with a focus on the key components of the simulation is shown in Fig. 2. Here, the robot, gripper and aircraft are visible, denoting the key components for contact force analysis. The following sections will address each of them with a general description of their individual characteristics.

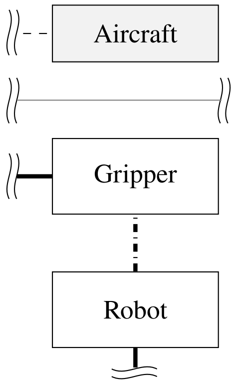

Fig. 2 Key components

3.2.1 Robot

The utilized industrial robot is a 6-axis serial kinematic robotic arm with a payload of 10 kg. Specifically, a Yaskawa HC10 DTP (Fig. 3a) combined with a Yaskawa YRC1000 micro robot controller. The robot consists of a serial chain of links connected by six actuated joints, reaching a spherical workspace with a radius of 1.37 m (without gripper attached). The six actuated axes are denoted as the S, L, U, R, B and T axis respectively, shown in Fig. 3a. Compared to other types of robots, a serial kinematic robot offers a larger workspace and higher manipulability. This facilitates both catching the aircraft and subsequent manipulation for further ground handling processes. However, the serial kinematic composition does also introduce singular configurations, preventing continuous movements through the workspace. In order to synchronize with the position of the UAV, the robot must be able to perform fast traversal motions within its workspace. A task space that fulfills this property was identified

Except where otherwise noted, content of this paper is licensed under a Creative Commons Attribution 4.0 International License.

The reproduction and distribution with attribution of the entire paper or of individual pages, in electronic or printed form, including any material under non-CC-BY 4.0 licenses is hereby granted by the authors and respective copyright owners.

in [14, p. 8]. By maintaining a certain robot configuration type, a sufficient non-singular region for the robot's task execution was found. The robot configuration type is defined by the arrangement of the joint axes to each other.

To communicate with the robot's controller an interface was created in [14, p. 7], allowing direct setpoint inputs to the axes' controller with a frequency of 250 Hz. Together with the robot's controller, the robot can be denoted as position controlled. The code, serving as an interface between the real-time host computer and the robot controller is publicly available as open source [15]. One limitation of the interface is that there is a delay of approximately 40 ms between each setpoint input being executed. Additionally, the robot's finite acceleration limitations impose further second order delay behavior. Fig. 3b shows an exemplary response of the robot's S-axis for a joint position ramp with an amplitude of 20°. The ramp corresponds to a speed step of $120\,^\circ\,\mathrm{s}^{-1}$. As described, the behavior resembles a step response of a damped $\mathrm{PT_2T_t}$ transfer function. The proprietary interface enforces maximum speed ratings of the individual joints, inducing nonlinear behavior.

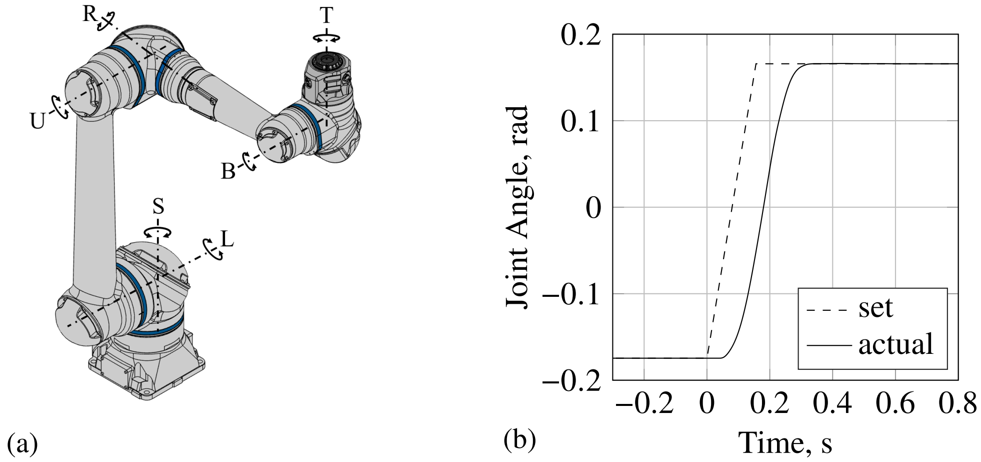

(a) (b)

Fig. 3 Properties of the robotic arm in (a) a rendering of the physical system and in (b) an exemplary response of the S-axis for a ramp with an amplitude of 20° and a speed of $120^\circ\ \mathrm{s}^{-1}$.

To model the utilized robot in a multi-body simulation, experimental data about the robot's system behavior is required to enable methods of system identification [16]. For that, the experimental data should be as informative as possible [16, p. 411]. Since impulse or step inputs are not applicable due to the physical limitations of the robot, ramp inputs with different amplitudes close to the maximum joint velocities were chosen. The experiments were conducted with the gripper attached, in close proximity to the initial configuration $q_{T_0} = (0, 0, 0, 0, 90^\circ, 0)^\mathrm{T}$ as shown in Fig. 3a, portraying a reasonable operating point, see [14, p. 8]. The joint position response was fed back by the robot's controller. Concurrently, an external optical tracking system was utilized to measure the gripper's Cartesian pose for validation purposes. During the experiments, the repetition accuracy was calculated, providing a comparative measure for model quality assessment. Additionally, a chirp signal was fed in for validation with a varying setpoint signal frequency of 0.1 Hz up to 2 Hz for all six axes simultaneously. Again different amplitudes were recorded. Further information on model identification will be described in Section 4.1.

3.2.2 Gripper

To catch the UAV in flight and provide assistance for further ground handling processes, a gripper is attached to the robot's end effector. The gripper's design was first presented in [14, p. 9]. Fig. 4a shows the original design of the attached gripper. The arms and base of the gripper are equipped with foam pads for a soft and secure grasp. The foam pads consist of a soft foam made from extruded ethylene propylene diene monomer (EPDM), a synthetic rubber. EPDM was chosen because of its solvent-resistance, environmental durability and high friction coefficient, which is advantageous for outdoor

Except where otherwise noted, content of this paper is licensed under a Creative Commons Attribution 4.0 International License.

The reproduction and distribution with attribution of the entire paper or of individual pages, in electronic or printed form, including any material under non-CC-BY 4.0 licenses is hereby granted by the authors and respective copyright owners.

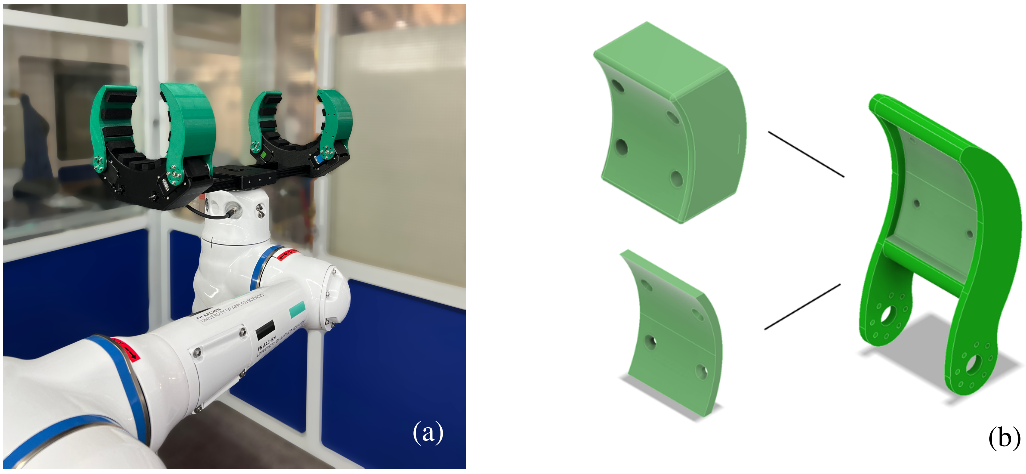

Fig. 4 Impressions on the gripper design with the previous gripper iteration in (a) and modifiable jaws for different UAV geometries in (b)

gripping applications. The area-specific stiffness of the utilized EPDM foams is summarized in Tab. 1. The servos (Dynamixel MX-106 by the company Robotis Co. Ltd.) of the four individually motorized arms allow for fast and torque-limited fixation of the UAV. To allow for different UAVs, modifiable gripper jaws were designed (Fig. 4b), offering the possibility to fit different UAV fuselage geometries. Upcoming iterations of the gripper will feature a modifiable base geometry to distribute the UAV's impact force on a larger surface area.

3.2.3 Aircraft

The aircraft in-use is a tilt-rotor VTOL with a wingspan of 2 m and a maximum takeoff weight (MTOW) of $m_{\mathrm{UAV}} = 3\,\mathrm{kg}$, provided by a project partner. Fig. 5 provides an impression on the utilized tilt-rotor VTOL in hover flight. The UAV features a light-weight 3D-printed fuselage, enabling fast iterations on fuselage geometry or accommodated hardware like radar reflectors but potentially increasing fragility. To mimic the behavior of a heavier and larger UAV in flight, a companion computer is available.

Fig. 5 Tilt-rotor VTOL in hover flight

4 Contact Force Simulation

To analyze contact forces during the robot assisted landing, a contact force simulation is designed. The considered scenario is depicted in Fig. 6. During the approach of the UAV, the robot performs a synchronization of movements in the horizontal plane, utilizing a model predictive controller. The UAV descends at a predefined constant vertical speed until it comes into contact with the gripper. Here, the simulation calculates resulting contact forces, the UAV's motors are shut down and the gripper is closed. Thus, the UAV "lands" on the gripper and the robot behaves according to it's specified joint elasticity. An approach with actively induced compliant behavior of the robot during the catch (as indicated by the

Except where otherwise noted, content of this paper is licensed under a Creative Commons Attribution 4.0 International License.

The reproduction and distribution with attribution of the entire paper or of individual pages, in electronic or printed form, including any material under non-CC-BY 4.0 licenses is hereby granted by the authors and respective copyright owners.

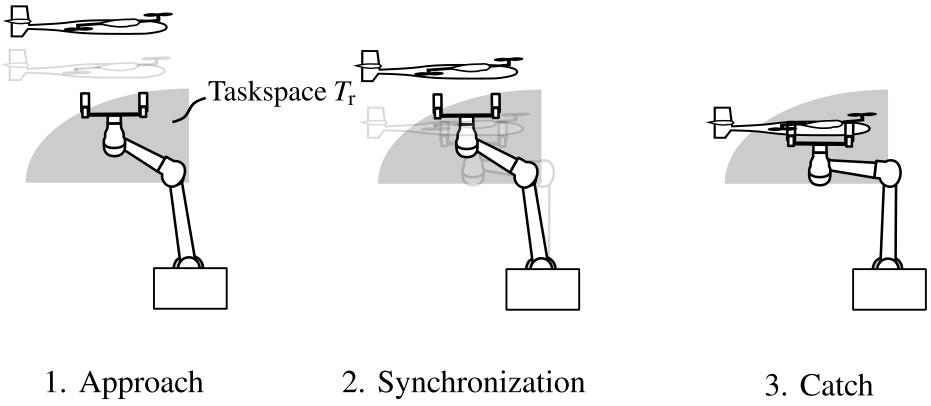

Fig. 6 Sequence of events for the simulated robot assisted landing

third picture in Fig. 6) is presented in the next section. The simulation of contact forces is implemented within the *Matlab/Simulink* environment, utilizing *Simscape*, a component-based modeling environment. This environment was chosen for its native support for multi-body simulation creation and execution. Furthermore, it incorporates built-in utilities for contact force calculation. The following section will present the modeling of the involved simulation components robot, gripper and aircraft respectively, proceeding with an explanation on utilized contact force calculation methods. After that, results of exemplary contact force simulations are analyzed and discussed.

4.1 Modeling involved components

To incorporate the involved components (i.e. robot, gripper and aircraft) into the simulation, models have to be derived, representing each system's characteristics as described in Section 3.2. During modeling, a balance must be found between a suitable model complexity for an accurate system representation and an efficient formulation with respect to required computation time. In the work presented, the robot is modeled based on system identification whereas the gripper and aircraft can be denoted as first-principles models.

4.1.1 Robot model

To transfer designed control concepts to the actual robot hardware easily, the simulation must be as representative as possible. For that, the robot's delay behavior as well as its elastic properties during contact situations need to be considered. The robot's model was identified utilizing the experimental data described in Section 3.2.1. Since the axes' behavior resembled a step response of a damped $\mathrm{PT_2T_t}$, the first approach was to estimate the model parameters of a second order delay element, utilizing the *System Identification Toolbox* by *Matlab*. However, compared to model structures with an increased number of model parameters such as higher order ARX (auto-regression with exogeneous variables) models [16, p. 11], the second order delay element has not proven sufficient. Whether a model was sufficient or not was quantified employing the repetition accuracy as a natural accuracy boundary. Fig. 7 portrays the standard deviation of the error distribution of the validation results for an ARX model of the robot's S-axis for different total model orders $N_\mathrm{a} + N_\mathrm{b}$. Here, N_a and N_b denote the number of past output and input terms used to predict the current output. The standard deviation is used as a measure of the model's prediction quality. Until a total model order of $N_\mathrm{a} + N_\mathrm{b} \approx 10$ is reached, the standard deviation declines, indicating an improvement in model prediction quality. A local minimum can be recognized at $N_\mathrm{a} + N_\mathrm{b} \approx 18$. Compared to the validation results of a damped $\mathrm{PT_2T_t}$, the ARX model has a lower standard deviation (by a factor of $\approx 4 \ldots 6$). Nevertheless, the second order delay model may prove helpful in future investigations when computation complexity is contemplated further (e.g. considering robot dynamics in an online model predictive controller).

Except where otherwise noted, content of this paper is licensed under a Creative Commons Attribution 4.0 International License.

The reproduction and distribution with attribution of the entire paper or of individual pages, in electronic or printed form, including any material under non-CC-BY 4.0 licenses is hereby granted by the authors and respective copyright owners.

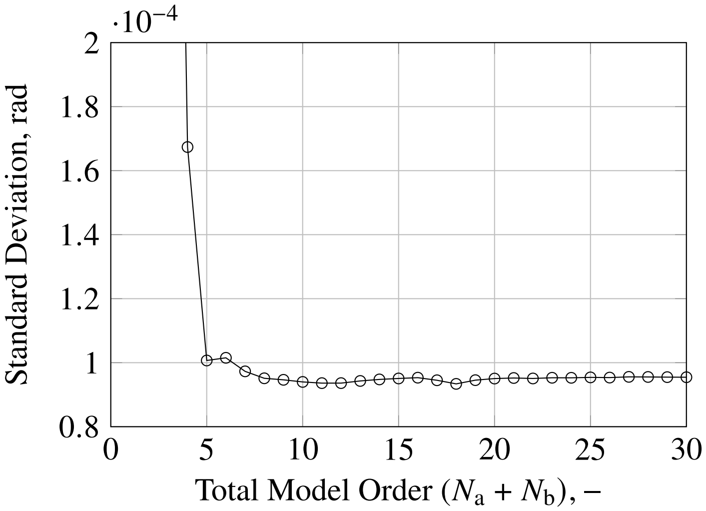

Fig. 7 Validation results for the ARX model of the robot's S-axis for different total model orders

Within *Simscape*, the robot is modeled as a multi-body system. Six revolute joints connect the robot's links which are endowed with corresponding mass and inertia properties based on a manufacturer's computer-aided design (CAD) model. Joint motion is imprinted based on external joint position commands considering the ARX model for each axis correspondingly. For each joint, the required torque for the imprinted motion is calculated. Additionally, external forces and torques propagating through the kinematic chain and acting on the joint are measured. By assuming the ARX model covers the robot's non-elastic behavior only, elasticity is introduced into the model with a series-connected torsion spring-damper system based on the required and external torque measurements.

4.1.2 Gripper model

Analogous to the robot, the gripper is modeled as a multi-body system as well, consisting of four revolute joints for the four motorized arms respectively. The gripper's components — the flange and the jaws — are imported from CAD. For contact force calculation, a collision geometry has to be defined. During the catching process, the flange's surface will serve as the main physical interface to the UAV. While *Simscape* offers the functionality to generate a convex hull over an imported CAD geometry to provide a corresponding collision geometry, the generated geometry is a coarse representation only and hence non-sufficient for replicating the gripper's foam contact surface. Therefore, to define the gripper's collision geometry, simple cuboid shapes are utilized representing the foam pads. As a result, contact forces are imposed on these collision geometries only, with one cuboid shape for the flange and four for the jaws respectively. This simplification is appropriate since numerous foam pads are spread across the gripper, covering the surface of the flange and the claws. The gripper is virtually connected to the robot by utilizing a reference coordinate system which is based on the current kinematic configuration of the robot.

4.1.3 Aircraft model

At the time of writing no flight model of the utilized UAV was available. Thus, a simplified UAV model, possessing a comparable inertia and geometry, was designed and utilized within the contact force simulation. In order to analyze the onset and magnitude of contact forces, accurately modeling the UAV dynamics is less important and hence a simplified UAV model is sufficient. During the catching process, the UAV's fuselage will serve as the main physical interface to the robot. The collision geometry of the UAV is defined as an ellipsoid shape representing the fuselage geometry. The UAV's motion is governed by four engines, placed in a quadcopter assembly. The engines produce thrust forces based on custom

Except where otherwise noted, content of this paper is licensed under a Creative Commons Attribution 4.0 International License.

The reproduction and distribution with attribution of the entire paper or of individual pages, in electronic or printed form, including any material under non-CC-BY 4.0 licenses is hereby granted by the authors and respective copyright owners.

PID controllers for velocity and attitude. The simplified model is able to maintain a configurable descent speed v_z.

4.2 Contact force calculation

To calculate the contact force between collision geometries, a simplified model for contact is required. Fig. 8a describes an approach where the contact between UAV and gripper is modeled as a linear spring-damper system, also known as linear Kelvin-Voigt contact model [13, p. 27]. Here, the spring-damper system represents the gripper's foam pads. Applying the linear Kelvin-Voigt contact model yields

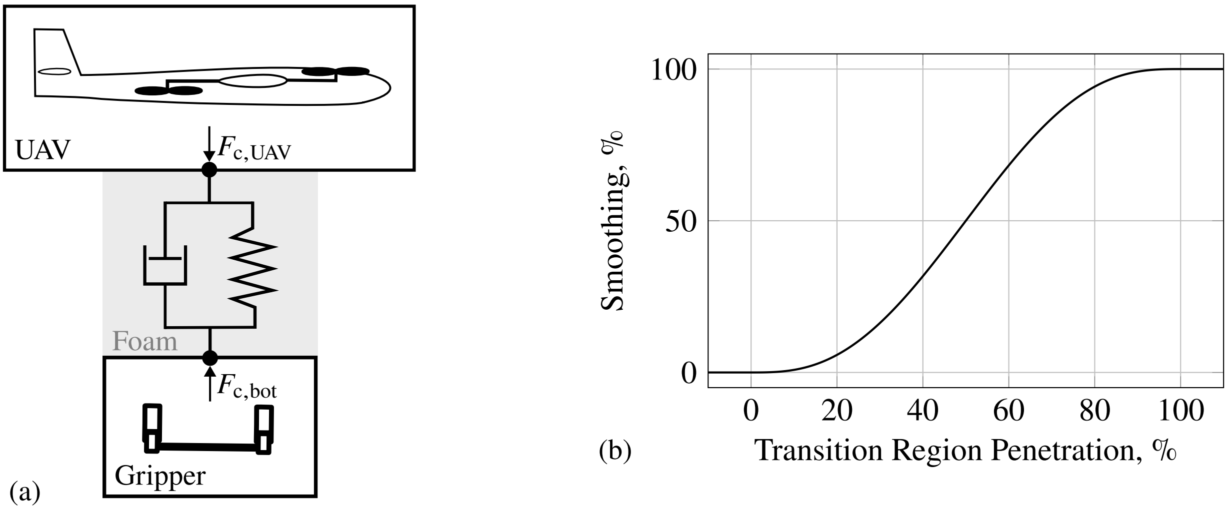

Fig. 8 Information on contact force calculation with (a) a simplified system representation, where the foam pads are modeled as a spring-damper system and (b) a plot of the smoothing function applied in the Kelvin-Voigt contact model. The plot is normalized with respect to the transition length.

$$F_{c,\mathrm{UAV}} = F_{c,\mathrm{bot}} = k \cdot x + c \cdot \dot{x} \tag{1}$$

with a spring stiffness k, a damping d and a penetration depth between two contacting geometries x. The applied forces on UAV and gripper are denoted as $F_{c,\mathrm{UAV}}$ and $F_{c,\mathrm{bot}}$ respectively. The spring stiffness k and damping d are characterized by the foam's material. This contact model type allows for an elastic as well as a dissipative interaction between the collision geometries. In *Simscape* a modified version of linear Kelvin-Voigt contact model is utilized [17], where

$$F_{c,\mathrm{UAV}} = F_{c,\mathrm{bot}} = s(x, w) \cdot (k \cdot x + c \cdot \dot{x}) \,. \tag{2}$$

Here, a smoothing function $s(x, w)$ is added, introducing a transition length w. Fig. 8b shows $s(x, w)$ for the ratio x/w, denoting the transition region penetration. If the penetration is within a preset transition length w, the calculated forces are smoothed by means of $s(x, w)$. The smoothing function ensures a smooth onset of forces to ensure physical plausibility and reduce numerical instabilities. Assuming $w \ll x_{\max}$, where $x_{\max}$ denotes the maximum penetration during contact, the contact force magnitude is not influenced by $s(x, w)$.

For simulation, reasonable values for the contact material's stiffness k and damping d must be specified. Since no reliable values for neither spring stiffness nor damping of the EPDM foam pads could be found in the literature, a simple approach for initial testing was adopted. To obtain an area-specific stiffness k_A, a force-displacement curve for a foam pad probe with a known surface area was recorded, utilizing ten values for the regressand. As a result, the area-specific stiffness k_A was determined for two different foam types (in the following denoted as hard and soft): $k_{\mathrm{A,hard}} = 0.02\,\mathrm{N\,mm^{-3}}$ and $k_{\mathrm{A,soft}} = 0.006\,\mathrm{N\,mm^{-3}}$ (summarized in Tab. 1). Theoretically, the spring stiffness needs to be calculated in each timestep of

Except where otherwise noted, content of this paper is licensed under a Creative Commons Attribution 4.0 International License.

The reproduction and distribution with attribution of the entire paper or of individual pages, in electronic or printed form, including any material under non-CC-BY 4.0 licenses is hereby granted by the authors and respective copyright owners.

Table 1 Measured values for area-specific stiffness k_A for utilized foams

Parameter	Value
$k_\mathrm{A,hard}$	$0.02\,\mathrm{N\,mm^{-3}}$
$k_\mathrm{A,soft}$	$0.006\,\mathrm{N\,mm^{-3}}$

the contact force simulation based on the current contact surface area and the area-specific stiffness k_A. However, for simplicity it is assumed that the contact between the UAV's fuselage ellipsoid and the gripper's flange occurs over a length of 500 mm (length of the modeled flange's surface) and a width of 1 mm . . . 3 mm (based on in-simulation observations). With the resulting area, the stiffness range can be calculated to $k_\mathrm{hard} = 10\,000\,\mathrm{N\,m^{-1}} \ldots 30\,000\,\mathrm{N\,m^{-1}}$ and $k_\mathrm{soft} = 3000\,\mathrm{N\,m^{-1}} \ldots 9000\,\mathrm{N\,m^{-1}}$ respectively. In addition to the spring stiffness, a damping coefficient d has to be defined. The damping coefficient d can be expressed as a function of the dimensionless damping ratio ζ [13, p. 38]:

$$d = 2 \cdot \zeta \cdot \sqrt{k \cdot m_\mathrm{UAV}} \tag{3}$$

Due to the lack of material information, three representative cases were considered to simulate different damping behavior:

- underdamped system: $\zeta < 1$
- critically damped system: $\zeta = 1$
- overdamped system: $\zeta > 1$

To analyze an underdamped or overdamped system, $\zeta = 0.5$ and $\zeta = 2$ were chosen respectively. Tab. 2 summarizes the resulting stiffness and damping coefficients.

Table 2 Calculated values for spring stiffness k and damping coefficient d (rounded)

k	$d_{\zeta=0.5}$	$d_{\zeta=1.0}$	$d_{\zeta=2.0}$
$30\,000\,\mathrm{N\,m^{-1}}$	$300\,\mathrm{N\,s\,m^{-1}}$	$600\mathrm{N\,s\,m^{-1}}$	$1200\,\mathrm{N\,s\,m^{-1}}$
$10\,000\,\mathrm{N\,m^{-1}}$	$200\,\mathrm{N\,s\,m^{-1}}$	$350\,\mathrm{N\,s\,m^{-1}}$	$700\,\mathrm{N\,s\,m^{-1}}$
$3000\,\mathrm{N\,m^{-1}}$	$100\,\mathrm{N\,s\,m^{-1}}$	$200\,\mathrm{N\,s\,m^{-1}}$	$400\,\mathrm{N\,s\,m^{-1}}$

4.3 Contact force analysis and discussion

After defining the contact force model and selecting appropriate stiffness and damping parameters, the resulting interaction forces are analyzed in simulation. While utilizing *Matlab/Simulink*, ordinary differential equations (ODEs) are employed to describe the time evolution of the simulation component's states. When a simulation exhibits widely separated time scales, the resulting equations are referred to as stiff ODEs. For contact force simulation, the UAV dynamics are characterized by substantially larger time scales than the contact force dynamics. In order to reduce the computation time and increase stability of the simulation, implicit integration methods, also known as stiff ODE solvers, with variable time steps are recommended [18, p. 1]. *Matlab* offers a wide variety of stiff ODE solvers [18]. For the simulation, *ode23s* was utilized which is based on a modified Rosenbrock formula [18, p. 7]. The solver automatically adjusts a time step length to handle stiff ODEs while maintaining a configurable maximum time step length of 4 ms. This solver was chosen since it showed superior results in comparison to other stiff ODE solvers for some example problems [19]. When comparing the available stiff ODE solvers for this particular problem, computation time differences were insignificant.

This section describes and discusses simulated results for the parameter variations' influence on the resulting contact force. The investigations include variations in the UAV's descent speed as well as

Except where otherwise noted, content of this paper is licensed under a Creative Commons Attribution 4.0 International License.

The reproduction and distribution with attribution of the entire paper or of individual pages, in electronic or printed form, including any material under non-CC-BY 4.0 licenses is hereby granted by the authors and respective copyright owners.

different values for the aforementioned spring stiffness and damping coefficient. Additionally, the propagation of contact forces through the robot's joints are analyzed.

4.3.1 Variation of descent speed

In the following, the landing process is simulated as depicted in Fig.6. Initially, variations of the descent speed are analyzed. For that, reasonable descent speed values are chosen based on prior investigations. In [14, p. 3], for ideal conditions, a final contact speed of approximately 0.03 - 0.05 $\mathrm{m\,s^{-1}}$ was observed. Accordingly, three different descent velocities (0.03 $\mathrm{m\,s^{-1}}$, 0.1 $\mathrm{m\,s^{-1}}$ and 0.2 $\mathrm{m\,s^{-1}}$) are simulated. Each simulation starts with the same initial height of 2.1 m for the UAV. Fig. 9 shows the resulting total contact force normal to the gripper flange's surface for a stiffness of $k = 10\,000\,\mathrm{N\,m^{-1}}$ and a damping ratio of $\zeta = 1$. As expected, the initial contact force is highest for the maximum descent speed of 0.2 $\mathrm{m\,s^{-1}}$ with approximately 65 N. After an initial peak, the force settles at approximately 30 N, corresponding to the UAV's weight. Since the gripper's pose is allowed to deviate from a horizontal orientation, a small force component acts in the gripper flange's surface direction which is not recognizable in Fig. 9. A second peak occurs after approximately 0.45 s when the gripper claws close and briefly move the UAV towards the gripper flange's surface. The modeled claws absorb a small force component through friction, additionally lowering the contact force on the gripper's flange. At lower descent speeds, the initial contact force peak shifts in time since the contact occurs later. The maximum peak for 0.1 $\mathrm{m\,s^{-1}}$ is approximately at 50 N, indicating a nonlinear relation between descent speed and initial contact force peak, probably introduced by the unchanged smoothing function $s(x, w)$.

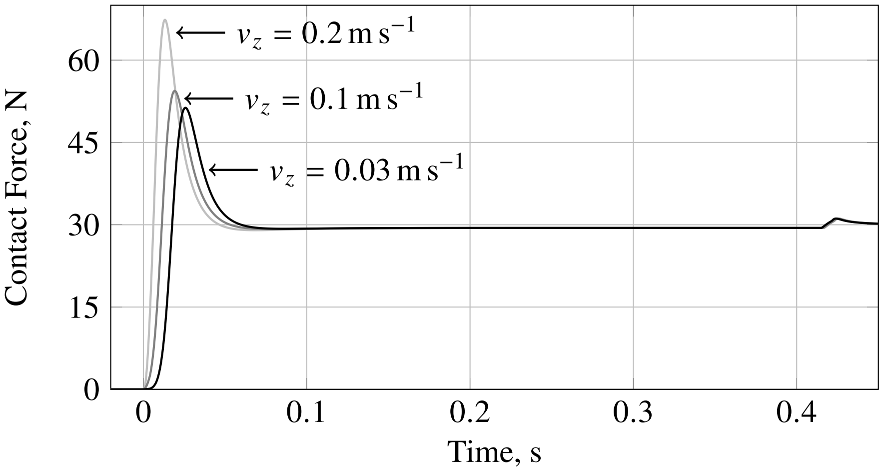

Fig. 9 Contact force normal to the gripper flange's surface with k = 10 000 N m^{-1} and ζ = 1 for different descent velocities. The time axis is normalized with respect to the time of contact.

4.3.2 Variation of spring stiffness and damping coefficient

In addition to the descent speed variation, a variation for the foam's spring stiffness is conducted. By maintaining a constant descent speed of $v_z = 0.03\,\mathrm{m\,s^{-1}}$ and a damping ratio of $\zeta = 1$, it can be observed that the initial contact force is highest for the stiffest spring (Fig. 10a). Thus, reducing the spring stiffness and hence simulating a softer material, results in a lower initial contact force peak. Regarding the subsequent decay of the contact force an inversely behavior is visible. The lower the spring stiffness, the longer it takes to dissipate the spring's energy (for a constant damping ratio) before settling at approximately 30 N. The results on spring stiffness variation are able to verify the simulation's plausibility.

To identify the influence of damping ratio variations, different foam damping ratios were analyzed (Fig. 10b). As expected, simulations with $\zeta = 0.5$ are underdamped and indicate oscillatory behavior. The damping coefficients $\zeta = 1.0$ and $\zeta = 2.0$ result in a response that converges to the settling force

Except where otherwise noted, content of this paper is licensed under a Creative Commons Attribution 4.0 International License.

The reproduction and distribution with attribution of the entire paper or of individual pages, in electronic or printed form, including any material under non-CC-BY 4.0 licenses is hereby granted by the authors and respective copyright owners.

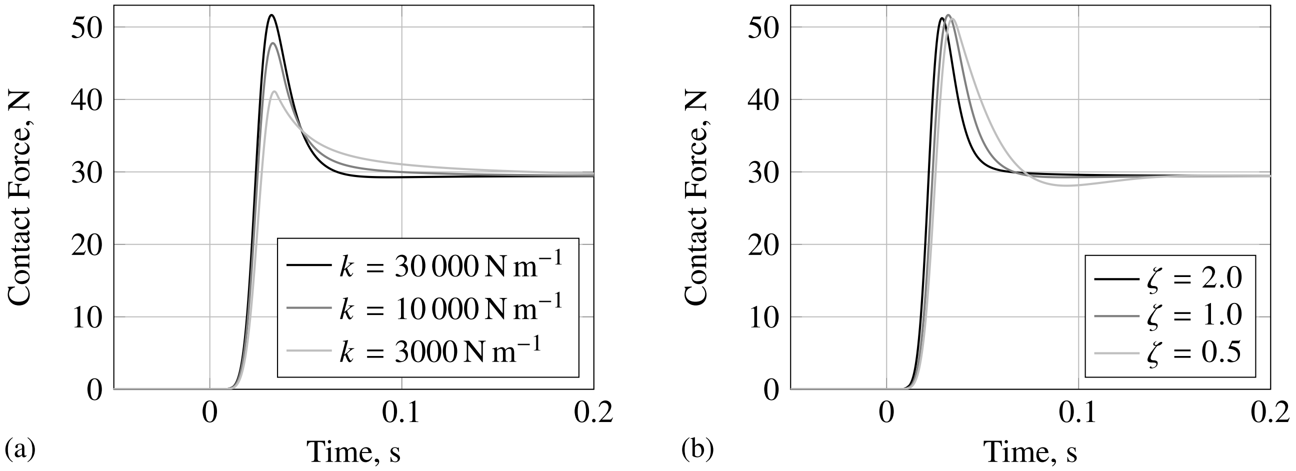

(a) (b)

Fig. 10 Contact force normal to the gripper flange's surface for a descent speed of v_z = 0.03 m s^{-1} in (a) for different spring stiffness values with ζ = 1 and in (b) for different damping coefficients with k = 30000 N m^{-1}. The time axis is normalized with respect to the time of contact.

of approximately 30 N asymptotically. Notably, the dependency on the chosen damping ratio ζ of the magnitude of the contact force seems to be negligible. A possible explanation may be the comparable small impact velocities between UAV and gripper, leading to a small amount of energy dissipation through damping during contact. However, for higher damping ratios, it is still recognizable that the contact force increases more rapidly.

4.3.3 Joint torque propagation

Since the modeled links of the robot possess inertia, the induced contact force is propagated through the kinematic chain. As described previously, external forces and torques may be measured on joint level individually, allowing a verification of the robot model. Fig. 11 shows the required torque for the imprinted motion during the robot assisted landing for the first two joints q_1 and q_2 respectively. The utilized robot configuration type is shown in picture Fig. 3a. At $t = 0$ s, a contact force is applied on the gripper, and propagated through the kinematic chain. Before contact, the required torque on q_1 is negligible, whereas q_2 is strained by the weight of subsequent robot links and the gripper. For $t > 0$ s, both q_1 and q_2 are loaded by the propagated contact force. However, the required joint torque for q_2 shows

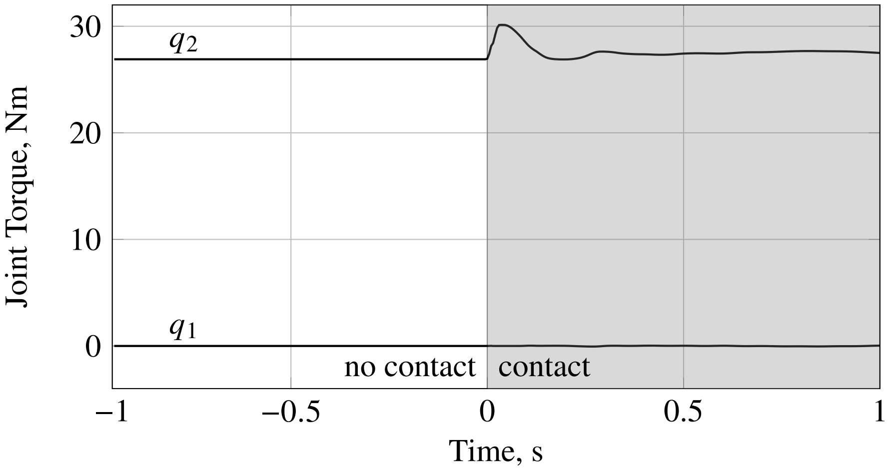

Fig. 11 Required robot joint torques during contact, exemplary shown for a joint which axis of rotation is parallel to the contact force, denoted as q_1, and for a joint which axis of rotation is perpendicular to the contact force, denoted as q_2. The time axis is normalized with respect to the time of contact.

Except where otherwise noted, content of this paper is licensed under a Creative Commons Attribution 4.0 International License.

The reproduction and distribution with attribution of the entire paper or of individual pages, in electronic or printed form, including any material under non-CC-BY 4.0 licenses is hereby granted by the authors and respective copyright owners.

significantly higher absolute values. Looking at the robot configuration type (Fig. 3a), the rotational axis of q_1 is approximately parallel to the direction of the modeled contact force (normal to the gripper flange's surface), whereas q_2 is approximately perpendicular to the direction of the modeled contact force. A force acting parallel to an axis of rotation does not generate a torque around that axis, resulting in a lower induced joint torque for q_1. Thus, by analyzing the joint torque propagation, the simulation's plausibility is verified.

5 Contact Force Reduction

To reduce the initial peak in contact force, the required deceleration of the UAV at impact needs to be reduced. The impact speed v_{rel}, denoting the relative speed between UAV and gripper at impact, represents a measure for the required deceleration. In order to reduce v_{rel} while the UAV's descent speed v_z is constant, the gripper needs to "descend" itself. As described in Fig. 6, within the simulation the robot performs a synchronization of movements in the horizontal plane while the UAV descends. A simple approach to impose a desired v_{rel} employs a prediction of the UAV's position. Assuming the UAV maintains a constant descent speed, the position at a prediction time T_{p} can be calculated, checking for a predicted contact onset. At the predicted contact onset, the robot receives a speed command of $v_{\text{bot}} = v_z - v_{\text{rel}}$ to impose a desired impact speed v_{rel}, accelerating within the modeled joint dynamics. Assuming $v_{\text{rel}} > 0$ and the robot's task space provides sufficient space for the desired movement, a contact will occur. At contact, the robot receives a speed command of $v_{\text{bot}} = 0\,\text{m}\,\text{s}^{-1}$, decelerating within the modeled joint dynamics.

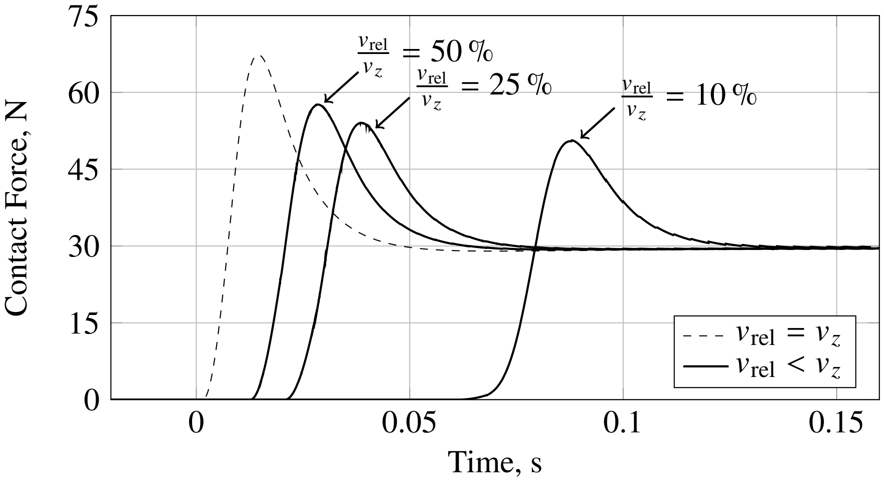

Fig. 12 Contact force normal to the gripper flange's surface for different impact velocities v_{rel} with a descent speed of v_z = 0.2 m s^{-1}, a spring stiffness of k = 10 000 N m^{-1} and a damping ratio of ζ = 1.

Fig. 12 visualizes the described procedure for different impact velocities v_{rel} and a prediction time T_{p} = 100 ms compared to a non-compliant robot behavior (dashed line) for a descent speed of $v_z = 0.02\,\text{m}\,\text{s}^{-1}$, a stiffness of $k = 10\,000\,\text{N}\,\text{m}^{-1}$ and a damping ratio of $\zeta = 1$. The desired impact speed v_{rel} is indicated

Table 3 Contact force and relative force reduction ΔF_{rel} for a descent speed v_z = 0.02 m s^{-1} (rounded)

$\frac{v_{\text{rel}}}{v_z}$	Contact Force	ΔF_{rel}
50 %	57 N	16 %
25 %	54 N	20 %
10 %	50 N	26 %

Except where otherwise noted, content of this paper is licensed under a Creative Commons Attribution 4.0 International License.

The reproduction and distribution with attribution of the entire paper or of individual pages, in electronic or printed form, including any material under non-CC-BY 4.0 licenses is hereby granted by the authors and respective copyright owners.

dependent on the descent speed v_z. By reducing v_{rel}, a reduction in contact force magnitude is evident. Table 3 shows the absolute contact forece and the relative force reduction ΔF_{rel} for an impact and descent speed ratio $\frac{v_{\text{rel}}}{v_z}$. The lower the impact speed, the later the impact occurs, since the robot ”descends” faster. Reducing the impact speed further will cause the robot to self-collide before making contact with the UAV. Thus, utilizing this procedure is limited by the available robot's task space. To incorporate these findings into the employed model predictive controller, a linear constraint (e.g. in a quadratic program) on velocity differences between UAV and gripper needs to be introduced in Cartesian space. The specification of an admissible contact force, and therefore the specific constraint on velocity differences, depends on which combination of heavier and larger UAV and robot is being investigated.

6 Conclusion

An approach on contact force simulation and subsequent reduction during robot-assisted landings of unmanned aerial vehicles was presented. The simulation allows the investigation of different combinations of unmanned aerial vehicles and industrial robots. To design a suitable contact force simulation, the key components' characteristics were identified, described and modeled. Subsequently, a multi-body simulation was implemented comprising the modeled key components as well as contact force calculation capabilities. Simulation results on variations of the UAV's descent speed and material parameters such as stiffness and damping were analyzed and verified. To reduce an initial contact force peak, an approach on reducing the impact speed was presented and discussed. By reducing the impact speed, the contact forces are reduced considerably.

In future investigations, measurement data by a dedicated test campaign will enable the validation of the contact force simulation. Furthermore, the approach on contact force reduction will be considered within the employed model predictive controller.

Acknowledgements

Our work has been conducted within the CatchUp project. This project is funded by the Federal Ministry of Transport (BMV) within the mFUND program. We thank all project partners for their work and contributions to the CatchUp project.

Bundesministerium
für Verkehr

mFUND
Das Startkapital für die Mobilität der Zukunft

Declaration of Use of Artificial Intelligence

Artificial intelligence was not used in the work presented.

References

[1] EULE - Europäische UAV-unterstützte Transport-Lösungen für Medizinische Güter. Retrieved 2025-10-28. `https://eule-mfund.de/`.

Except where otherwise noted, content of this paper is licensed under a Creative Commons Attribution 4.0 International License.

The reproduction and distribution with attribution of the entire paper or of individual pages, in electronic or printed form, including any material under non-CC-BY 4.0 licenses is hereby granted by the authors and respective copyright owners.

[2] Yavor Dobrev, Marten Schütt, Philipp Hartmann, and Dieter Moormann. Entwurf und Validierung eines Präzisionslandesystems für unbemannte Tiltwing-Fluggeräte. In *Luft- und Raumfahrt - Hochtechnologie aus Deutschland : Deutscher Luft- und Raumfahrtkongress 2016 : 13.-15. September 2016, Braunschweig / DGLR*. Deutsche Gesellschaft für Luft- und Raumfahrt - Lilienthal-Oberth e.V., 2016.

[3] Luis Gustavo Leandro de Paula, Vijay Shankar Dwivedi, Hyo-Sang Shin, and Antonios Tsourdos. A review on vtol autonomous landing strategies on naval dynamic surfaces. In *Proceedings of the 2024 CEAS EuroGNC conference*. Bristol, UK, June 2024. doi: https://doi.org/10.82124/CEAS-GNC-2024-048.

[4] Moritz Maier and Konstantin Kondak. Landing of vtol uavs using a stationary robot manipulator: A new approach for coordinated control. In *2015 54th IEEE Conference on Decision and Control (CDC)*, page 1497–1502, Osaka, Dec. 2015. IEEE. doi: 10.1109/cdc.2015.7402422, `http://ieeexplore.ieee.org/document/7402422/`.

[5] Moritz Maier, Andre Oeschger, and Konstantin Kondak. Robot-assisted landing of vtol uavs: Design and comparison of coupled and decoupling linear state-space control approaches. *IEEE Robotics and Automation Letters*, 1:114–121, Jan. 2016. ISSN: 2377-3766, 2377-3774. doi: 10.1109/LRA.2015.2502920.

[6] Moritz Maier and Konstantin Kondak. Robot assisted landing of vtol uavs on ships: A simulation case study of the touch-down phase. In *2017 IEEE Conference on Control Technology and Applications (CCTA)*, pages 2094–2101, 2017. doi: 10.1109/CCTA.2017.8062762.

[7] Moritz Maier and Konstantin Kondak. Landing of vtol uavs using a stationary robot manipulator: A new approach for coordinated control. In *2015 54th IEEE Conference on Decision and Control (CDC)*, page 1497–1502, Osaka, Dec. 2015. IEEE. doi: 10.1109/cdc.2015.7402422, `http://ieeexplore.ieee.org/document/7402422/`.

[8] Yimou Wu and Mingyang Liang. Robot-assisted drone recovery on a wavy surface using error-state kalman filter and receding horizon model predictive control, 2025. doi: 10.48550/arXiv.2505.09145, `https://arxiv.org/abs/2505.09145`.

[9] Quantum Systems. FreeRail mFUND Projekt- Gleisinspektion mittels UAS. Retrieved 2025-07-07. `https://www.youtube.com/watch?v=iMkI_P5Za_A&ab_channel=QuantumSystems`.

[10] Romeo Leo, Angelo De Fenza, M. Barile, and L. Lecce. Drop test simulation for an aircraft landing gear via multi-body approach. *Archive of Mechanical Engineering*, Volume 61, 08 2014. Retrieved 2025-09-30. doi: 10.2478/meceng-2014-0017.

[11] Steve Miller. Landing gear model in simscape, 2025. Retrieved 2025-09-20. `https://www.mathworks.com/matlabcentral/fileexchange/47534-landing-gear-model-in-simscape`.

[12] Xinlei Ni, Qiaozhi Yin, Xiaohui Wei, Peilin Zhong, and Hong Nie. Research on landing stability of four-legged adaptive landing gear for multirotor uavs. *Aerospace*, 9(12), 2022. Retrieved 2025-09-30. doi: 10.3390/aerospace9120776.

[13] Paulo Flores and Hamid M. Lankarani. *Contact Force Models for Multibody Dynamics*. Springer, 2016. ISBN: 978-3-319-30896-8.

[14] Vincent Konnow, Jannes Terlau, Lukas Hildebrand, and Philipp Hartmann. Robot assisted landing process of small uavs using decentralized kalman filter. In *Proceedings of the 2024 CEAS EuroGNC conference*. Bristol, UK, June 2024. doi: 10.82124/CEAS-GNC-2024-084.

[15] V. Konnow. Motoman ROS2, 2022. `https://github.com/adv4ncr/motoman_ROS2`.

[16] Lennart Ljung. *System Identification: Theory for the User, 2nd ed.* Prentice Hall PTR, 1999. ISBN: 0-13-656695-2.

Except where otherwise noted, content of this paper is licensed under a Creative Commons Attribution 4.0 International License.

The reproduction and distribution with attribution of the entire paper or of individual pages, in electronic or printed form, including any material under non-CC-BY 4.0 licenses is hereby granted by the authors and respective copyright owners.

[17] MathWorks. Spatial Contact Force, 2025. Retrieved 2025-09-23. `https://de.mathworks.com/help/sm/ref/spatialcontactforce.html`.

[18] Lawrence F. Shampine and Mark W. Reichelt. The matlab ode suite. *SIAM Journal on Scientific Computing*, 18(1):1–22, 1997. doi: 10.1137/S1064827594276424.

[19] MathWorks. ode23s, 2025. Retrieved 2025-09-26. `https://de.mathworks.com/help/matlab/ref/ode23s.html`.

Except where otherwise noted, content of this paper is licensed under a Creative Commons Attribution 4.0 International License.

The reproduction and distribution with attribution of the entire paper or of individual pages, in electronic or printed form, including any material under non-CC-BY 4.0 licenses is hereby granted by the authors and respective copyright owners.